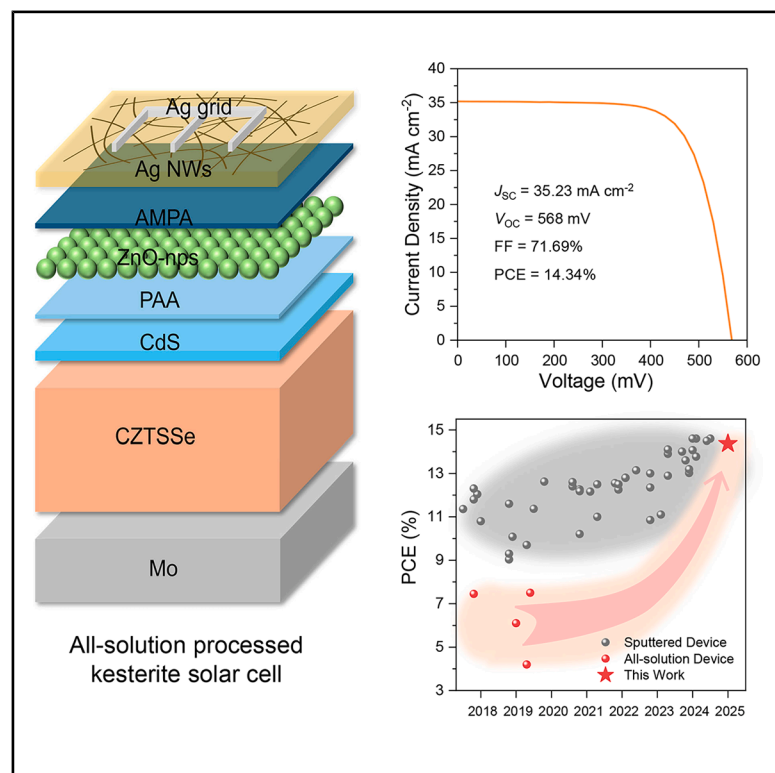


# Multi-interface engineering for all-solution-processed kesterite solar cells

## Graphical abstract



## Authors

Licheng Lou, Jinlin Wang, Yuan Li, ..., Yanhong Luo, Dongmei Li, Qingbo Meng

## Correspondence

shijj@iphy.ac.cn (J.S.),  
iamhxin@njupt.edu.cn (H.X.),  
qbmeng@iphy.ac.cn (Q.M.)

## In brief

Molecular engineering has been introduced to regulate the multiple interfaces of solution-processed ZnO nanoparticles (ZnO-nps)/Ag nanowires (AgNWs) window layers used for kesterite solar cells, aiming at improving interface contact, eliminating defects, and promoting charge transfer. This has enabled us to achieve 14.3% certified efficiency and excellent flexibility in the all-solution-processed kesterite solar cells. This achievement provides a critical technical foundation to support the low-cost and simpler preparation of thin-film solar cells in future commercialization.

## Highlights

- High-performance all-solution-processed kesterite solar cells were fabricated
- Multi-interface molecular engineering was implemented
- The device achieves record PCE of over 14% and excellent flexible performance

Article

# Multi-interface engineering for all-solution-processed kesterite solar cells

Licheng Lou,<sup>1,7</sup> Jinlin Wang,<sup>1,7</sup> Yuan Li,<sup>1</sup> Kang Yin,<sup>1</sup> Xiao Xu,<sup>1</sup> Bowen Zhang,<sup>1,2</sup> Menghan Jiao,<sup>1,2</sup> Shudan Chen,<sup>1,2</sup> Tan Guo,<sup>1,3</sup> Jingchen Wang,<sup>1,2</sup> Yiming Li,<sup>1</sup> Jiangjian Shi,<sup>1,\*</sup> Huijue Wu,<sup>1</sup> Ruijuan Xiao,<sup>1</sup> Hao Xin,<sup>4,\*</sup> Yanhong Luo,<sup>1,2,5</sup> Dongmei Li,<sup>1,2,5</sup> and Qingbo Meng<sup>1,2,5,6,8,\*</sup>

<sup>1</sup>Beijing National Laboratory for Condensed Matter Physics, Renewable Energy Laboratory, Institute of Physics, Chinese Academy of Sciences, Beijing 100190, P.R. China

<sup>2</sup>School of Physical Sciences, University of Chinese Academy of Sciences, Beijing 100049, P.R. China

<sup>3</sup>College of Materials Science and Optoelectronic Technology, University of Chinese Academy of Sciences, Beijing 100049, P.R. China

<sup>4</sup>State Key Laboratory of Organic Electronics and Information Displays and Institute of Advanced Materials, Nanjing University of Posts & Telecommunications, Nanjing 210023, P.R. China

<sup>5</sup>Songshan Lake Materials Laboratory, Dongguan 523781, P.R. China

<sup>6</sup>Center of Materials Science and Optoelectronics Engineering, University of Chinese Academy of Sciences, Beijing 100049, P.R. China

<sup>7</sup>These authors contributed equally

<sup>8</sup>Lead contact

\*Correspondence: [shijj@iphy.ac.cn](mailto:shijj@iphy.ac.cn) (J.S.), [iamhxin@njupt.edu.cn](mailto:iamhxin@njupt.edu.cn) (H.X.), [qbmeng@iphy.ac.cn](mailto:qbmeng@iphy.ac.cn) (Q.M.)

<https://doi.org/10.1016/j.joule.2025.102091>

**CONTEXT & SCALE** As climate change intensifies and global reliance on fossil fuels becomes increasingly unsustainable, the transition to clean energy has escalated to a critical imperative. Solar energy, characterized by its abundance and renewability, stands at the forefront of this transformation, with continuous advancements in accessibility and efficiency. Among emerging technologies, thin-film solar cells utilizing kesterite absorbers demonstrate significant promise due to their flexibility, cost-effectiveness, and utilization of earth-abundant elements, thereby mitigating material scarcity concerns. For widespread deployment, scalable manufacturing and cost efficiency are essential. However, fabrication bottlenecks persist, particularly in producing critical transparent conductive layers, which typically require capital-intensive vacuum deposition techniques. These processes constrain production scalability and economic viability. Consequently, investigating feasible and economical solution-processed production methodologies for these cells is vital to expanding clean energy access. Advancing such techniques represents a critical technological pathway toward enabling broader global adoption of solar power.

## SUMMARY

The interface contact issue, surface defects, and energy level mismatches have significantly limited the optoelectronic performance of solution-processed transparent conductive window layers for use in thin-film solar cells. In this work, these challenges are systematically addressed by employing molecular engineering to regulate the multiple interfaces of ZnO nanoparticles (ZnO-nps)/silver nanowires (AgNWs) window layers in kesterite solar cells. The interface molecular engineering enhances the conformal deposition of ZnO-nps on rough  $\text{Cu}_2\text{ZnSn}(\text{S}, \text{Se})_4$  (CZTSSe)/CdS substrates, passivates hydroxyl defects in ZnO-nps, and optimizes energy level alignment at the ZnO-nps/AgNWs interface. These advancements enable us to achieve a certified total area efficiency of 14.3%, marking a significant milestone for all-solution-processed kesterite solar cells. Furthermore, the solution-processed window layer forms a robust and flexion-tolerant lateral conductive network, imparting excellent flexibility to the cells. This development provides a critical technical foundation to support the low-cost and simpler preparation of thin-film solar cells in future commercialization.

## INTRODUCTION

Kesterite  $\text{Cu}_2\text{ZnSn}(\text{S}, \text{Se})_4$  (CZTSSe) thin-film solar cells have attracted significant attention due to their advantages, including

abundant elemental reserves, environmental friendliness, and high material stability.<sup>1,2</sup> Efforts over the past few years have seen the photoelectric conversion efficiency of these cells reach the commercial threshold of 15% through solution-fabricated

CZTSSe absorbers,<sup>2–4</sup> positioning them as a promising candidate for the future photovoltaic market. Transparent window layers are a key component of kesterite solar cells, playing crucial roles in charge collection and transport.<sup>5–7</sup> These layers, generally as ZnO/indium tin oxide (ITO), ZnO/ZnO:Al, or ZnO/In<sub>2</sub>O<sub>3</sub>:Zn, are primarily fabricated using vacuum deposition techniques, especially sputtering methods.<sup>8</sup> However, sputtering processes typically entail substantial capital investment in equipment, and the sputtering-induced damage significantly restricts the space of interface regulation.<sup>9,10</sup> These limitations impact the cost-effectiveness and potential application scenarios of kesterite solar cells, thereby affecting their competitiveness in future commercialization.

Researchers have been exploring convenient solution-based processes for preparing window layers, ultimately realizing the fabrication of CZTSSe solar cells through all-solution processes.<sup>9</sup> Among these, composite window layers consisting of ZnO nanoparticles (ZnO-nps) and silver nanowires (AgNWs) have garnered special attention due to their excellent transparent conductive properties and ease of film coating.<sup>5,11–13</sup> However, despite these advantages, the efficiency of CZTSSe solar cells based on this solution-processed technology has yet to surpass 10%, significantly lagging behind the continually improving sputtering-based cells.<sup>14–17</sup> This performance gap is also evident in other photovoltaic and optoelectronic devices.<sup>11,18,19</sup> The fundamental origin of the performance disparity between sputtering and solution-processed technologies lies in their distinct material systems, wherein the solution-processed nanocomposite film system intrinsically exhibits complex surface and interface structures, which are often associated with serious defects<sup>20,21</sup> and energy level mismatches,<sup>22</sup> hindering carrier transport and collection.<sup>23</sup> Furthermore, these films frequently struggle to achieve conformal deposition, especially on rough surfaces, which impacts the quality of the contact between multilayer films within the devices.<sup>24</sup> Effectively addressing these intertwined issues, including interface contact, carrier recombination, and energy level mismatch, is crucial for achieving high-performance solution-processed window layers for solar cells yet remains a significant challenge.

In this work, multiple interfaces within solution-processed ZnO-nps/AgNWs window layers were systematically engineered to optimize optoelectronic performance for use in kesterite solar cells. The multi-interface regulation strategy involves (1) using polyacrylic acid (PAA) as a surface binder to achieve conformal deposition of a ZnO-nps layer on the rough CZTSSe/CdS surface, (2) introducing aminomethylphosphonic acid (AMPA) molecules on the ZnO-nps surface to passivate surface defects, and (3) exploiting the permanent dipole of AMPA molecules to improve the energy level match at the ZnO-nps/AgNWs interface. These regulations realize high-performance ZnO-nps/AgNWs window layers with excellent charge collection, transport, and significantly reduced charge loss. This enables the all-solution-processed CZTSSe cell to achieve a significant breakthrough, reaching 14.3% certified efficiency. In addition, the overlapping AgNWs form a robust surface conductive network, which maintains excellent lateral charge transport ability even when the polycrystalline film substrate fractures, allowing the flexible CZTSSe solar cells to exhibit superior bending

stability. These results demonstrate that through multi-interface engineering, the optoelectronic performance of the solution-processed window layer has surpassed that of traditional sputtering-based window layers. This achievement opens new pathways for the low-cost and high-efficiency fabrication of thin-film solar cells.

## RESULTS AND DISCUSSION

### All-solution-processed CZTSSe solar cell

The device structure of the CZTSSe solar cell in our study is shown in [Figures 1A and 1B](#), in which all the functional layers were fabricated by solution methods. In particular, the conventional sputtering-deposited ZnO/ITO window layer was replaced by ZnO-nps and AgNWs layers deposited by solution-coating methods ([Figure S1](#)); the conventional Ni/Al grid electrode was replaced by a screen-printed Ag paste electrode. As in the cross-sectional scanning electron microscope (SEM) image shown in [Figure 1B](#), the coating-deposited ZnO-nps layers exhibit compact morphology and interface contact covering on the undulating surface of CZTSSe/CdS film. In the top-view SEM image, the overlapping AgNWs can also be clearly seen covering the ZnO-nps layer. Production efficiency and cost at the lab scale were further compared for the window layer using the all-solution processes (AS) to that based on the vacuum sputtering method (VAC). It was found that the fabrication time can be reduced by a factor of 5 and that the equipment and material consumption costs can be reduced by a factor of 10 ([Figure 1C](#); [Tables S1 and S2](#)). Preliminary cost estimates conducted under industrial production conditions also demonstrate a cost advantage for the all-solution-processed window layers ([Table S3](#)). This advantage would facilitate the development of a simpler device preparation process with a lower technical threshold and thus can provide a more easily achievable technical platform for systematic optimization of kesterite solar cells.

In experiments, the size of ZnO-nps and AgNWs were optimized and, in the final device, 40 nm ZnO-nps and 35 nm AgNWs with a length-to-diameter ratio of about 700 were used, respectively ([Figures S2 and S3](#)). Through these material and film deposition process optimizations, the composite window layer has exhibited excellent transparent and conductive properties. In a wide wavelength region from visible (400 nm) to infrared (1,200 nm), the transmittance of the film was comparable with that of the sputtered ITO film, with sheet resistance being controlled <25  $\Omega/\text{sq}$  ([Figure 1D](#)), enabling the cell to have an optical current density of over 43  $\text{mA cm}^{-2}$ , even without the anti-reflection (AR) layer.<sup>25</sup> After the basic optimization, interfaces within these all-solution-processed functional layers were investigated and engineered. Specifically, a thin PAA layer was introduced at the CdS/ZnO-nps interface to gain better heterogeneous covering and conformal deposition; AMPA molecules were utilized at the ZnO-nps/AgNWs interface to passivate the ZnO-nps surface defects and, moreover, facilitate the charge transfer. In the following sections, the challenges associated with fabricating kesterite solar cells based on all-solution-processed window layers will be sequentially illustrated, along with their resolution through multi-interfacial engineering.

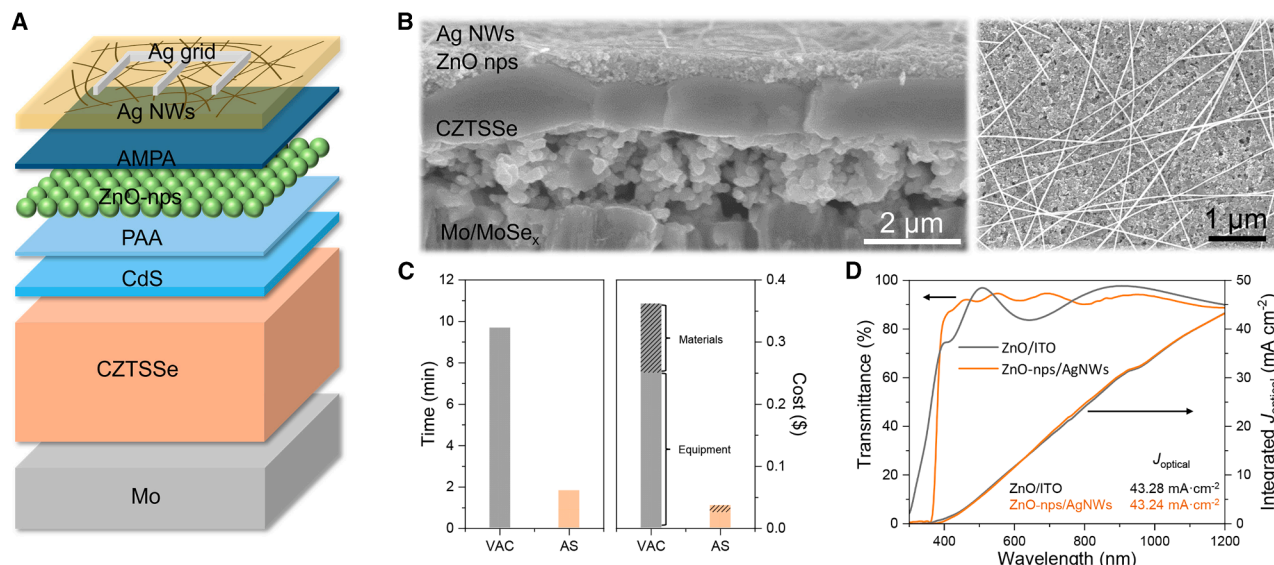


**Figure 1. All-solution-processed CZTSSe solar cell**

(A and B) (A) The schematic structure and (B) cross-sectional and top-view SEM image of the kesterite solar cell with all-solution-processed ZnO-nps/AgNWs window layers (AS device).

(C) Comparison of the preparation time and cost for the window layers fabricated by sputtering or AS process at the lab scale (averaged to a single cell). The detailed data are shown in [Tables S1](#) and [S2](#).

(D) Transmittance spectra of sputtered ZnO/ITO and solution-fabricated ZnO-nps/AgNWs window layers. The ideal current density ( $J_{\text{optical}}$ ) is calculated according to the transmittance spectra and 100% internal quantum efficiency.

### Conformal deposition of a ZnO-nps layer on a rough CZTSSe/CdS surface

The first challenge is to realize a conformal deposition of ZnO-nps onto the CZTSSe/CdS film surface because it is usually very rough. As shown in [Figures 2A](#) and [2B](#), when the ZnO-nps directly coated onto the film, most nanoparticles were accumulated in the low-lying area of the surface and those higher surfaces can barely be covered, resulting in significant reduction in surface roughness of the film. This could arise because the ZnO-nps aqueous solution has relatively large polarity and surface tension<sup>24,27</sup> and thus, in its drying process, exhibited significant shrinkage on the CdS surface with low surface energy. This could lead to direct exposure of the CZTSSe/CdS surface, which would not only introduce severe charge recombination in the cell but also corrode the AgNWs through Ag-S reactions ([Figure S4](#)).<sup>28–31</sup>

To address this issue, a PAA interfacial layer was introduced ([Figure S5](#)). The PAA was chosen from several organic molecules or polymer materials that had been tried in our experiment ([Figures S6](#) and [S7](#)). In particular, this is because PAA is a kind of polymer binder, having rich carboxyl groups that are able to have strong interactions with metal oxide nanoparticles.<sup>24,32</sup> Liquid contact angle measurements found that the PAA obviously enhanced the surface tension,<sup>33</sup> especially the polarity component, of the CdS layer, which thus improved the spreadability of the ZnO-nps aqueous solution ([Figures 2C](#) and [S8](#); [Table S4](#); [Note S1](#)). These effects finally helped the undulating CZTSSe/CdS surface to be conformally covered by ZnO-nps, thus maintaining the original film surface roughness as shown in [Figures 2A](#) and [2B](#).

This improvement resulted in an obvious reduction in the interfacial charge recombination, as reflected by the significantly enhanced photovoltage decay lifetime ([Figure 2D](#)).<sup>34,35</sup> In addition, photoluminescence (PL) spectra showed that CdS in the PAA-involved sample (CdS/PAA/ZnO-nps) exhibited a much lower steady-state PL intensity and shorter PL decay lifetime than that of the CdS/ZnO-nps sample ([Figures 2E](#) and [2F](#)), demonstrating that the improvement in the interfacial covering and contacting enhanced the carrier transfer at the CdS/ZnO-nps interface. This enhancement can reduce the carrier localization in the band-tail states of the chemical-bath-deposited CdS layer,<sup>36</sup> thus helping suppress performance loss of the cell. Further, current-voltage (*I*-*V*) measurements indicated that the heterojunction property of CZTSSe/CdS/ZnO-nps has also been improved. As in [Figures 2G](#) and [S9](#), when CdS was directly contacted with AgNWs window layer, an ideality factor (*A*, in [Note S2](#)) as large as 3.18 was observed. This parameter value was reduced to 2.22 by directly depositing a ZnO-nps layer; nonetheless, it still exceeded the general range of ideality factors for a single heterojunction, i.e.,  $1 \leq A \leq 2$ .<sup>26</sup> Comparatively, when the PAA was used, the ideality factor was reduced to 1.59, with a much lower reverse saturation current density, indicating the formation of an effective heterojunction. With these benefits to the CdS/ZnO-nps interface, the average efficiency of kesterite solar cells, based on the PAA-modified all-solution processes, was improved from ~10% to ~12.8% ([Figures S10–S12](#)).

### Surface defect passivation of ZnO-nps

Another challenge is related to the ZnO-nps itself because ZnO-nps synthesized from aqueous solutions generally have many



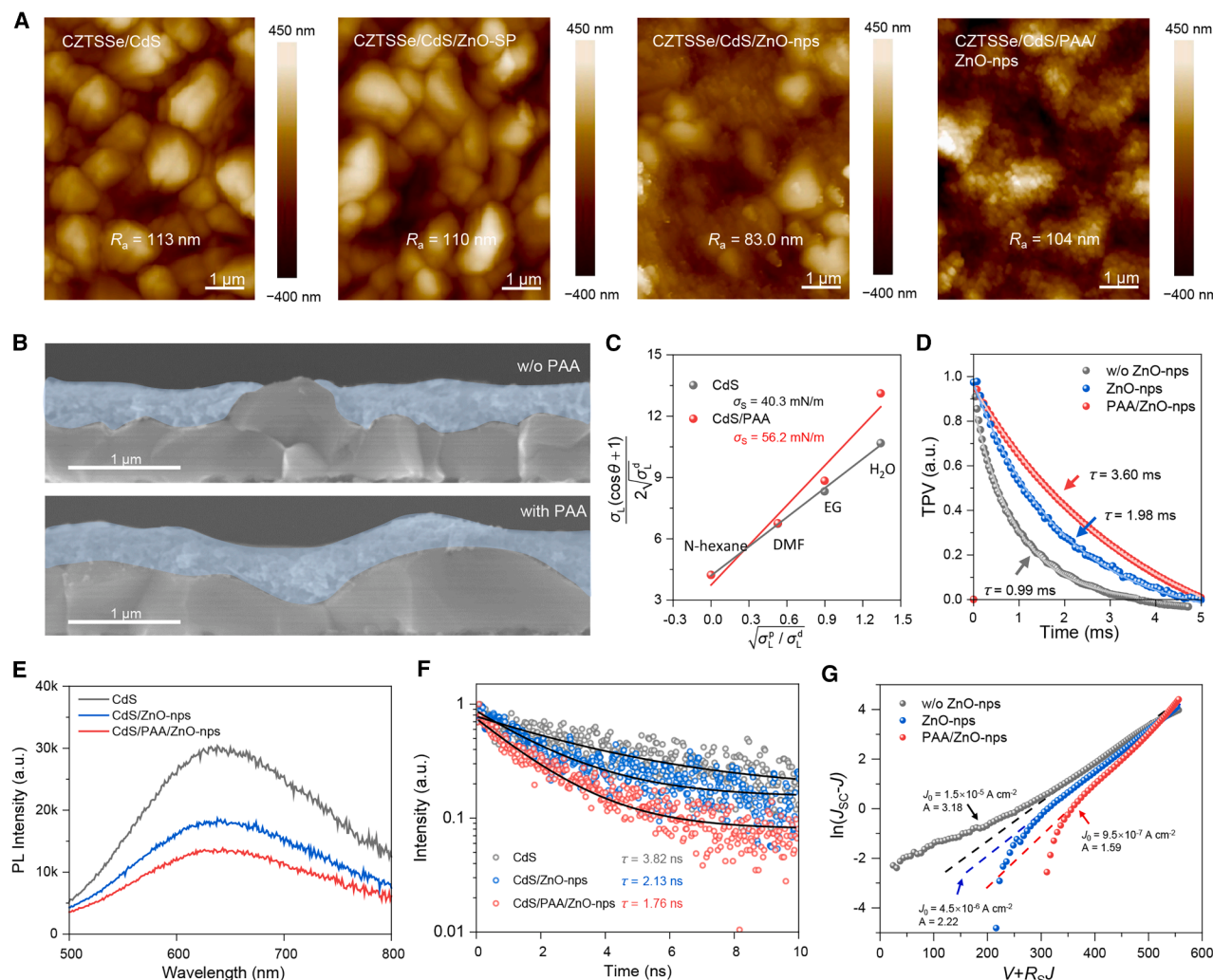


**Figure 2. Engineering of the CdS/ZnO-nps interface**

(A) Atomic force microscopy (AFM) image of CZTSSe/CdS, CZTSSe/CdS/ZnO (sputtered), CZTSSe/CdS/ZnO-nps, and CZTSSe/CdS/PAA/ZnO-nps films. (B) Cross-sectional SEM images of CdS/ZnO-nps interface with or without PAA regulation. (C) Surface energy analysis for CdS and CdS/PAA films. (D) Transient photovoltage of the cell without ZnO-nps, with ZnO-nps, and with PAA/ZnO-nps layers. (E and F) (E) Steady-state and (F) transient photoluminescence of CdS, CdS/ZnO-nps, and CdS/PAA/ZnO-nps films excited at 445 nm. (G) Ideality factor ( $A$ ) and reverse saturation current ( $J_0$ ) of the cells derived from  $I$ - $V$  curves.<sup>26</sup>

deep surface defects caused by the residue of hydroxyl groups.<sup>20</sup> Here, driven by the esterification mechanism, amino-phosphonic acid molecules were introduced on the surface of ZnO-nps to react with these hydroxyl groups. Through comparison, the AMPA, which has a shorter carbon chain, exhibited better interface modification performance, providing the highest cell efficiency (Figures S13–S15). As predicted by density functional theory (DFT) calculations (Figure 3A), by releasing a  $H_2O$  molecule as well as a total energy of about 2.16 eV, the AMPA would bind to the ZnO surface. The occurrence of this reaction was demonstrated by Fourier transform infrared (FTIR) spectra in which the signal located at about  $3,300\text{ cm}^{-1}$ , corresponding to the stretching vibration of hydroxyl groups, disappeared after the AMPA treatment,<sup>37</sup> indicating effective removal of the detri-

mental hydroxyl groups (Figure 3B). Meanwhile, a new vibration band centered at about  $1,076\text{ cm}^{-1}$ ,<sup>38</sup> corresponding to the stretching vibration of Zn-O-P, appeared in the ZnO-nps/AMPA sample, indicating the transformation from Zn-O-H to Zn-O-P-N structures, as depicted in Figure 3A. The multi-peak fitting of O 1s and Zn 2p X-ray photoelectron spectroscopy (XPS) also supported the removal of hydroxyl groups and the appearance of this new structure (Figures 3C and S16).<sup>39</sup>

However, despite the atomic structure transformation of the ZnO surface, the DFT calculations found that the distribution of density of states of ZnO did not obviously change and, in particular, that the defect states in the forbidden gap still existed (Figure S17). That is, chemical passivation of the surface defects was not realized, probably because the surface Zn was still

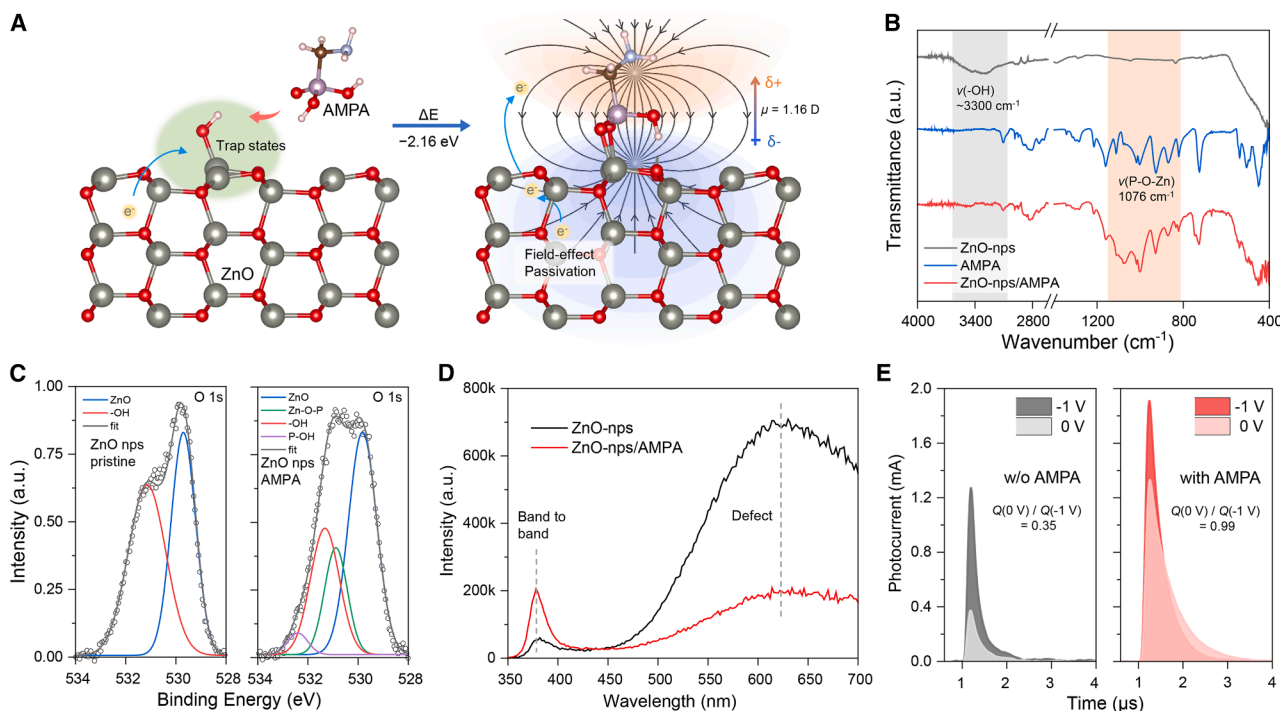


**Figure 3. Surface defect passivation of ZnO-nps**

(A) DFT-simulated reaction between AMPA molecule and  $\text{-OH}$  on ZnO-nps surface. The reaction diminishes the  $\text{-OH}$  group and induces a dipole forming on the surface in which the electric field direction is schematically shown by black arrows.  
 (B) FTIR spectra of ZnO-nps, AMPA, and ZnO-nps/AMPA powders collected from deposited films.  
 (C) XPS of O 1s for ZnO-nps and ZnO-nps/AMPA films.  
 (D) Steady-state PL spectra of ZnO-nps and ZnO-nps/AMPA films.  
 (E) Bias-voltage-dependent transient photocurrent characteristics of the cells with or without the AMPA modification.

linked to excessive oxygen atoms. Nonetheless, it was found that through the Zn-O-P-N structures, a permanent dipole with a magnitude of 1.16 D formed perpendicular to the ZnO-np surface, in which the negative charge was located closer to the surface, as shown in Figure 3A. The formation of this dipole was confirmed by surface work function measurement using Kelvin probe force microscopy (KPFM, Figures 4A and 4B), which showed that the value of work function of the ZnO-nps film decreased by about 280 meV after the AMPA treatment.

This permanent dipole forms a local electric field in the surface region, electrostatically repulsing electrons transported in the ZnO-nps away from the defect position that is forming field-effect passivation toward those point defects.<sup>40,41</sup> This passivation effect was confirmed using steady-state PL measurement. As in Figure 3D, for the pristine ZnO-nps, a significant defect emission band at about 620 nm was observed under the ultraviolet excitation. After AMPA treatment, the defect emission was reduced by about 4-fold and the band-to-band emission of ZnO-nps at about 375 nm was significantly enhanced, indicating reduced carrier trapping and defective emission. In the solar cell, this can reduce the defect-assisted carrier loss.<sup>42,43</sup> Photocurrent decay (Figure 3E) and external quantum efficiency (EQE) (Figure S18) of the solar cells measured under different bias voltages also supported this result. For the pristine ZnO-nps-based cell, significant charge loss was observed when the external bias

voltage changed from  $-1$  V to 0 V. This arose because  $-1$  V could provide a considerably large electric field to extract the photo-generated electrons, reducing its capture by the surface defects, whereas, under 0 V, most of the photo-generated electrons were captured by these surface defects. In contrast, after the AMPA treatment, this charge loss phenomenon was almost completely eliminated, implying that the ZnO-nps-induced electron capturing has been effectively passivated.

### Band alignment improvement of the ZnO-nps/AgNWs interface

Energy band matching is also a critical requirement for the fabrication of high-efficiency solar cells. Through band-edge position measurements (Figures 4A, 4B, and S19–S21; Note S3), a mismatch in the conduction band minimum (CBM) was found between ZnO-nps and the AgNWs. As shown in Figure 4C, CBM of the ZnO-nps was 0.16 eV lower than that of the AgNWs, which hinders the fast transfer of electrons across this interface. Interestingly, it was found that the dipole introduced by the AMPA improved the energy band alignment of this interface. Specifically, the negative charge in the dipole raised the CBM position of the ZnO-nps, thus eliminating the energy barrier at this interface.

This improvement helped in obtaining an Ohmic contact at the ZnO-nps/AgNWs interface, as demonstrated by the  $I$ - $V$

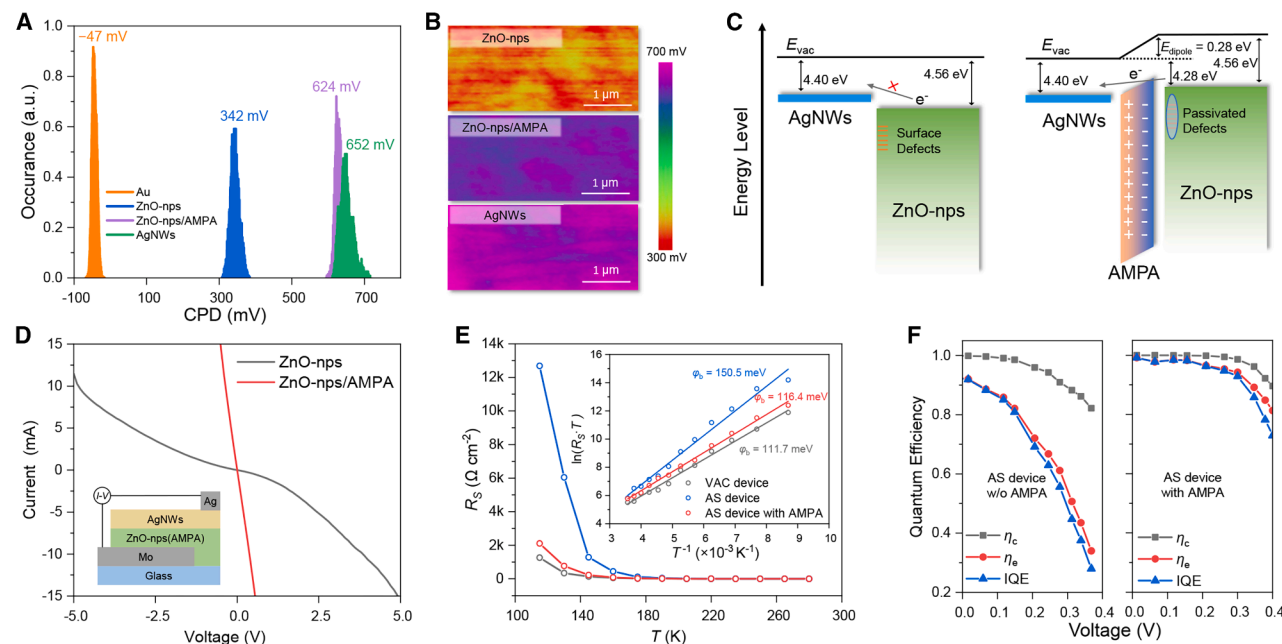


**Figure 4. Energy band alignment and charge transport at the ZnO-nps/AgNWs interface**

(A and B) (A) Contact potential difference (CPD) distribution and (B) mapping images of ZnO-nps, ZnO-nps/AMPA, and AgNWs films on the CZTSSe/CdS substrate, measured using KPFM.

(C) Energy band diagram of ZnO-nps/AgNWs interface with or without the AMPA-induced dipole.

(D) *I*-*V* curve of a junction (inset diagram) comprised of Mo/ZnO-nps/AgNWs/Ag.

(E) Temperature-dependent series resistance ( $R_s$ ) of the sputtered cell and the AS cell with or without AMPA modification. The inset figure shows the Arrhenius plots to derive the energy barrier ( $\phi_b$ ) of charge transport.

(F) The carrier collection efficiency ( $\eta_c$ ), extraction efficiency ( $\eta_e$ ), and internal quantum efficiency (IQE) of the AS cell with or without the AMPA modification.

characteristics measurement of a junction comprised of Mo/ZnO-nps/AgNWs/Ag. As in Figure 4D, the *I*-*V* curve of the unmodified junction shows an obvious charge transport barrier, whereas the straight *I*-*V* curve of the modified sample demonstrated that this barrier has been effectively reduced. When fabricated into a complete solar cell, this improved interfacial charge transport led to an obvious reduction in the series resistance ( $R_s$ , shown in Figure 4E). Especially at low temperatures, the  $R_s$  decreased by about 4-fold, and reached a level comparable with that of the sputtered device. Temperature-dependent  $R_s$  measurement further showed that the equivalent energy barrier for the interfacial charge transfer decreased from 150 to 116 meV (Note S4).<sup>44</sup> Further investigation using modulated transient photocurrent/voltage (m-TPC/TPV) measurements revealed a significant improvement in the internal quantum efficiency (IQE, Figure 4F; Note S5) of the device, showing an enhanced carrier utilization.<sup>34,45</sup> Finally, the benefits of AMPA, including field-effect passivation and energy level alignment improvement, resulted in a considerable reduction in the charge loss in the cell and thus helped us further improve the average efficiency of the cell from 12.8% to about 14.0% (Figures S10 and S22).

### Device performance of rigid and flexible kesterite solar cells

With these efforts, high photoelectric conversion performance of all-solution-processed solar cells has been realized (Figure 5A). The average cell efficiency is even a little higher than that of

the sputtered device, implying that the overall optoelectronic performance of the all-solution-processed window and grid electrode layer has surpassed that based on conventional vacuum processes. In particular, our cell achieved a certified total area efficiency of 14.34%, with short-circuit current density ( $J_{sc}$ ) of 35.23 mA·cm<sup>-2</sup>, open-circuit voltage ( $V_{oc}$ ) of 568 mV, and fill factor (FF) of 0.717 (Figures 5B, S23, and S24), which is almost double that of previously reported all-solution-processed devices (7.51%; Figure 5C).<sup>11,15,17</sup> Compared with the sputtered device, our cell here exhibited significantly enhanced  $V_{oc}$ , which, on one hand, benefited from the reduced sputtering-induced damage<sup>42,46</sup> and, on the other hand, was a result of the reduced interface charge recombination through multi-interface engineering. Moreover, our device exhibits excellent performance in the 300-s maximum power point tracking (MPPT) test (Figure S25), and no observable performance degradation was detected after 6 months of ambient storage (Figure S26), demonstrating superior stability.

Furthermore, these all-solution technologies were used to fabricate flexible kesterite solar cells on a molybdenum foil substrate (Figure S27). As shown in Figure 5D, the cell obtained a high efficiency of 13.12%, also comparable with that of the sputtered flexible cell, and has also reached the highest result reported so far (Table S7).<sup>47,48</sup> In addition to the efficiency, the flexible cell demonstrated excellent bending performance. When bent at different radii, ranging from 25 to 5 mm (Figure S28), little efficiency change was observed in the all-solution-processed

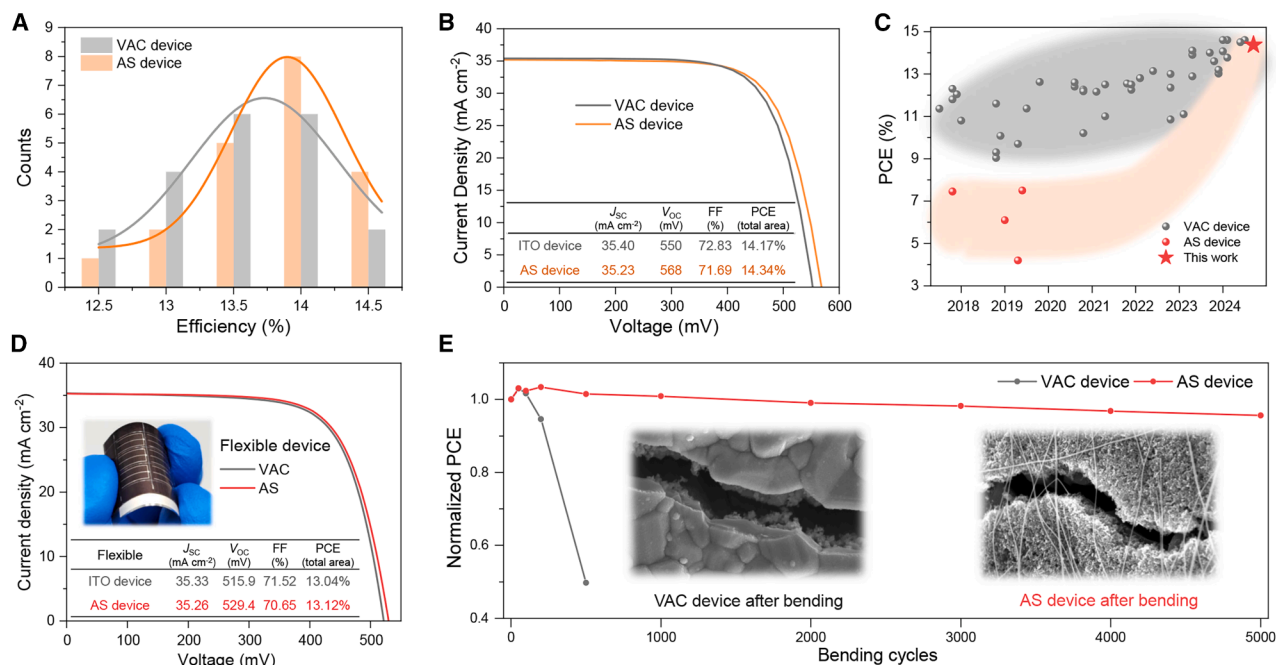


**Figure 5. Device performance of all-solution-processed rigid and flexible kesterite solar cells**

(A) Efficiency distribution of VAC devices and AS devices. The AS devices employed both PAA and AMPA modification.

(B) *I*-*V* curves of champion solar cells with the window layer fabricated by conventional sputtering or by the solution method.

(C) Efficiency progress of different types of kesterite solar cells in recent years. The detailed performance data are shown in [Tables S5](#) and [S6](#).

(D) *I*-*V* curve of champion flexible cells.

(E) Bending performance of these two types of flexible cells, bent for various cycles at a bending radius of 8 mm. The inset SEM figures are sputtered and AS device after being bent for 500 and 5,000 cycles, respectively.

cell, whereas an obvious efficiency decline appeared in the sputtered cell when it was bent at 15 mm. Furthermore, the all-solution-processed cell can sustain 95% of its initial efficiency after being bent 5,000 times at a bending radius of 8 mm ([Figure 5E](#)), which is superior compared with previous work ([Table S8](#)). However, the efficiency decline of the sputtered cell had exceeded 50% after being bent just 500 times. This significant performance difference in flexibility primarily lies in the influence of bending on the lateral charge transport. For the sputtered cell, bending caused cracks in the ITO film, which significantly damaged the lateral charge transport of the cell, whereas, for the all-solution-processed cell, although cracks also appeared after the bending, the long AgNWs form a robust surface conductive network that can still connect the domains separated by these cracks ([Figure 5E](#)), thus assuring the lateral charge transport and collection. The bending test was also conducted on the ZnO-nps/ITO structure device ([Figures S28](#) and [S29](#)), which exhibited significantly inferior bending performance compared with the AS device. This reaffirms that the intrinsic flexibility and robust lateral charge transport ability of the AgNWs is pivotal for enhancing the bending performance of solar cells.

Through the aforementioned multi-interface regulations, CZTSSe solar cells fabricated via all-solution processes have achieved efficiency levels comparable with those of conventional devices (VAC device) and superior advantages in flexible device application. This accomplishment primarily stems from

the expansive material selection offered by solution-based processes for interface modification, enabling us to tailor and optimize materials based on the specific characteristics of each interface. Consequently, this solution-processed window layer technique exhibits compatibility with diverse absorber/buffer layer substrates, such as the CZTS absorber and a cadmium-free ZnSnO buffer layer.<sup>49</sup>

Moving forward, to enable large-area production of kesterite solar cells, the future research focus of all-solution-based processing lies in achieving scalable coating deposition for different functional layers. In the current study, blade coating fabrication of the window layers (ZnO-nps/AgNWs) has been successfully demonstrated. However, scalable coating for the CZTSSe precursor film remains under exploration.<sup>50,51</sup> Both blade and slot die coating technologies should be developed for realizing the large-area deposition of CZTSSe precursor layers. Additionally, the development of controllable and large-scale selenization methods is desired for CZTSSe absorber fabrication.<sup>52</sup> These manufacturing advancements, synergizing with performance-enhancing strategies like selenization design,<sup>53</sup> defect regulation,<sup>3,4</sup> energy band engineering,<sup>54,55</sup> and alternative buffer layer development,<sup>49,56</sup> will collectively promote the commercialization of CZTSSe solar cells.

## Conclusions

In this work, all-solution-based device fabrication technology has been applied to enhance the cost-effectiveness and



potential application scenarios of kesterite solar cells. Particularly, molecular engineering has been employed to regulate the multiple interfaces of solution-processed ZnO-nps/AgNWs window layers to improve cell performance. Our approach has enhanced the conformal deposition of ZnO-nps on rough CZTSSe/CdS substrates, passivated hydroxyl defects in ZnO-nps, and also optimized energy level alignment of the ZnO-nps/AgNWs interface, which significantly improved the charge transport and reduced charge loss in the cell. These benefits have helped us to achieve a certified total area efficiency of 14.3% in the all-solution-processed kesterite solar cells, marking a significant advancement in this field. Furthermore, the solution-processed window layer forms a robust and flexion-tolerant lateral conductive network, imparting excellent flexibility to CZTSSe cells. Overall, our work provides a valuable pathway for the more cost-effective and efficient manufacturing of high-performance kesterite solar cells, which will contribute to accelerating the industrialization of these cells through technological diversification.

## METHODS

### Materials

CuCl (99.999%) was purchased from Alfa Aesar; PAA ( $M_w = 450,000$ ),  $\text{SnCl}_4$  (99.998%), polyvinyl pyrrolidone (PVP,  $M_w = 58,000$ ), and ethylene glycol (99.7%) from Macklin; AgCl (99.5%) and PVP ( $M_w = 1,300,000$ ) from Innochem; and Zn ( $\text{CH}_3\text{COO}$ )<sub>2</sub> (99.99%), ZnO-nanoparticle solution (40% in water), AMPA (97%), thiourea (99.99%), 2-methoxyethanol (MOE, 99.8%), 1-Butanol (99.5%), and  $\text{CdSO}_4 \cdot 8/3\text{H}_2\text{O}$  (99.99%) from Aladdin. Se pellets (99.999%) were purchased from Zhong Nuo Advanced Material;  $\text{NH}_4\text{Cl}$  (99.5%) and ammonium hydroxide (25.0%~28.0%) from Sinopharm Chemical Reagent Co. Ltd.; and  $\text{Zn}(\text{CH}_3\text{COO})_2 \cdot 2\text{H}_2\text{O}$  (AR),  $\text{AgNO}_3$  (AR), NaCl (AR), and KBr (AR) from Xilong Chemical Co. Ltd. Silver paste (01L-2210) was purchased from Shenzhen Sryeo Electronic Paste Co., Ltd. Thiourea was used after two recrystallization, and other chemicals were used directly without further purification.

### Fabrication of the CZTSSe absorber

The precursor solution was prepared as follows: 1.083 g CuCl, 1.469 g  $\text{Zn}(\text{CH}_3\text{COO})_2$ , 1.9815 g  $\text{SnCl}_4$ , and 3.656 g thiourea were dissolved in 15 mL MOE, then stirred at 60°C for 1 h; 0.1725 g AgCl and 0.0937 g  $\text{CdCl}_2$  were finally dissolved in the above solution for another 1 h to achieve the final colorless solution. The molar ratios of  $\text{Ag}/(\text{Ag} + \text{Cu})$ ,  $(\text{Ag} + \text{Cu})/(\text{Zn} + \text{Sn})$ ,  $\text{Zn}/\text{Sn}$ , and thiourea/metal are 0.1, 0.75, 1.12, and 1.7, respectively. The concentrations of metal elements and thiourea are 1.88 and 3.20 mol/L, respectively. Mo substrates ( $4 \times 4 \text{ cm}^2$ ) were first cleaned by deionized (DI) water, then treated with UV-ozone for 15 min for better solution wettability. There was no extra treatment for Mo substrates. CZTSSe precursor films were prepared by spin-coating the precursor solution on Mo substrates at 3,200 rpm/s for 25 s in the air, followed by annealing for 150 s on a 280°C hot plate in the air. The coating and annealing processes were repeated 7 times for the desired 1.2- to 1.5- $\mu\text{m}$ -thick precursor films. Finally, a CZTSSe absorber layer was obtained by annealing as-prepared precursor films at 540°C for

1,200 s with  $\text{N}_2$  flow in a selenium-contained graphite box, which was put inside the selenization furnace at one standard atmospheric pressure.

### Fabrication of CdS buffer layer

A 40-nm-thick CdS buffer layer was then fabricated by chemical bath deposition method: 0.0612 g  $\text{CdSO}_4 \cdot 8/3\text{H}_2\text{O}$ , 0.1280 g  $\text{NH}_4\text{Cl}$ , 0.7288 g thiourea, and 10.5 mL ammonium hydroxide were added in 200 mL DI water and stirred for dissolution. Then, the CZTSSe films were immersed in the above solution and kept in the 70°C water bath for 11 min.

### Fabrication of vacuum-based devices

A device configuration with Mo/CZTSSe/CdS/ZnO/ITO/Ni/Al was fabricated based on the above-prepared CZTSSe/CdS layer. An intrinsic ZnO and ITO window layer was deposited by radio-frequency magnetron sputtering. Then, a 2- $\mu\text{m}$ -thick Ni/Al collection grid layer was thermally evaporated. The total area of each solar cell is designed to be 0.28  $\text{cm}^2$  in our lab measurement.

### Fabrication of AgNWs

17 mL of ethylene glycol and 0.668 g of PVP ( $M_w = 1,300,000$ ) are placed in a clean three-necked flask and stirred in a 170°C oil bath until completely clear, while nitrogen is bubbled to maintain an inert atmosphere. Dissolve 10 mg KBr and 20 mg NaCl in 1.5 mL of ethylene glycol, then pour into the three-necked flask. Dissolve 0.2793 g of  $\text{AgNO}_3$  in 1.5 mL of ethylene glycol, then slowly add into the three-necked flask. Maintain at 170°C in an oil bath for 2 h with a stirring speed of 200 rpm. Afterward, quickly cool the three-necked flask in an ice water bath. Then, purify using the acetone precipitation method. Add 60 mL of deionized water to the mixture obtained above, then slowly pour in about 100 mL of acetone and stir slowly. The solution gradually stratifies and a brown precipitate appears. After standing for 1 h, remove the upper layer of liquid, add 40 mL of 0.5% PVP ( $M_w = 58,000$ ) aqueous solution to the precipitate, and stir to form a uniform dispersion. Then, continue adding acetone and repeat the above process three times. The final AgNWs precipitate is dispersed in 40 mL of ethanol, centrifuged at 1,000 rpm for 3 min, and the upper liquid is collected. Continue to centrifuge at 4,000 rpm for 7 min, collect the bottom precipitate, redisperse it in isopropanol, and finally prepare around 3 mL AgNWs dispersion with a concentration of about 6 mg/mL.

### Fabrication of all-solution-based devices

The device with configuration of Mo/CZTSSe/CdS/PAA/ZnO-nps/AMPA/AgNWs/Ag was fabricated based on the above-prepared CZTSSe/CdS layer. PAA solution was prepared by dissolving 2 mg PAA in 1 mL DI water and stirring overnight. ZnO-nps dispersion was prepared by diluting the commercial ZnO-nps water dispersion into 80 mg/mL in DI water, ultrasonically for 10 min, and finally filtering with 800-nm filters. The AMPA solution was prepared by dissolving 1 mg AMPA in 1 mL DI water. The AgNWs solution was prepared by diluting the as-prepared AgNWs isopropanol dispersion into 2 mg/mL with butanol. Then, the four layers of PAA, ZnO-nps, AMPA, and AgNWs were doctor-bladed with a substrate temperature

of 80°C. The size of doctor blade coating is 4 cm × 4 cm, which includes four 2 cm × 2 cm solar cells. The blade heights were 400, 400, 400, and 200 μm, respectively. The blade speeds were 4, 8, 4, and 6 mm/s, respectively. Each time, 100 μL of the solution was used. The annealing conditions were 1, 10, 1, and 1 min at 120°C in the air, respectively. The Ag electrode was made by screen-printing, with a height of 10 μm and a width of around 60 μm, and was further annealed in the air at 120°C for 10 min. A 360-mesh stainless steel wire screen was employed, with a wire angle of 22.5° and a tension of 23 N. The screen mask pattern is illustrated in [Figure S30](#), and the optimization conditions of the screen-printed electrode are illustrated in [Figures S31](#) and [S32](#). Then, the device was annealed at 180°C for 60 min in a nitrogen atmosphere. The single cell was obtained by mechanical scribing and the total area of the cell was designed to be about 0.29 cm<sup>2</sup>.

### Characterization

SEM images were measured on Hitachi S4800 SEM using 10 kV power. The ultraviolet-visible (UV-vis) diffuse reflectance spectrum was recorded on a Shimadzu UV-3600 spectrophotometer. X-ray diffraction (XRD) patterns were obtained on an X-ray diffractometer with Cu Kα as the radiation source (Empyrean, PANalcal). Contact angles were obtained by OCA25, DataPhysics. Current density-voltage (*J*-*V*) curve of cells were collected on a Keithley 2400 Source Meter under AM 1.5G illumination (100 mW cm<sup>-2</sup>) from a solar simulator (Zolix SS160A). The intensity of the light source was calibrated by a standard silicon solar cell certified by National Institute of Metrology, China (NIMC). The reference cell was certified by NIMC. The measurement was performed at room temperature (25°C) in air, with a scanning rate of about 90 mV·s<sup>-1</sup> from -0.05 to 0.6 V. m-TPC/TPV spectra were obtained by our lab-made setup in which the cell was excited by a 532-nm pulse laser (Brio, 20 Hz, 4 ns) and the photovoltage decay process was recorded by a digital oscilloscope (Tektronix, DPO 7104). Steady-state and transient state PL spectra were obtained from a PL spectrometer (Edinburgh Instruments, FLS 900). The XPS measurement was carried out on an ESCALAB 250Xi (Thermo Fisher) instrument. EQE was obtained from Enlitech QE-R test system with a xenon lamp and a bromine tungsten lamp as light sources. Ultraviolet photoelectron spectroscopy is measured by Thermo Scientific ESCALAB250Xi. KPFM images were obtained on Bruker, Multi-mode 9. FTIR spectroscopy was performed on a TENSOR 27 spectrometer, Bruker. Temperature-dependent *J*-*V* curves from 100 to 290 K were measured on an electrochemical workstation (Princeton, Versa STAT) and cooled down with liquid nitrogen.

### First-principle calculations

Our spin-polarized DFT calculations were conducted using the Vienna *ab initio* simulation package (VASP), leveraging plane-wave basis sets in conjunction with the projector augmented-wave method.<sup>3,4</sup> The exchange-correlation energy was tackled using the generalized gradient approximation (GGA), with the Perdew-Burke-Ernzerhof (PBE) functional serving as the parameterization framework. To overcome GGA's inherent shortcomings, methodology was refined by integrating a GGA + U

approach. The effective Hubbard *U* parameter was judiciously selected as 7.5 eV for zinc. Further enhancing the validity of our calculations, we introduced Van der Waals forces consideration via Grimme's DFT-D3 model. To simulate the intricate interactions between individual molecules and the ZnO (10-10) surface, our model comprised quintuple layers arranged into a 2 × 2 surface cell. A generous 20 Å vacuum buffer was instituted to effectively isolate the slab and mitigate any erroneous periodic image interactions. The plane-wave energy cutoff was judiciously set at 450 eV. For the integration over the Brillouin zone, we opted for a  $\Gamma$ -centered Monkhorst-Pack mesh of 3 × 2 × 1. The upper two layers of the slab and the molecule adsorbed thereon were allowed to relax until the forces converged below 0.02 eV/Å, with an energy convergence criterion set at 10<sup>-5</sup> eV. Consistent across all system evaluations, dipole corrections were meticulously applied to address potential surface effects meticulously.

### RESOURCE AVAILABILITY

#### Lead contact

Requests for further information and resources should be directed to and will be fulfilled by the lead contact, Qingbo Meng ([qbmeng@iphy.ac.cn](mailto:qbmeng@iphy.ac.cn)).

#### Materials availability

This study did not generate new unique reagents.

#### Data and code availability

All data reported in this paper will be shared by the [lead contact](#) upon request.

### ACKNOWLEDGMENTS

This work has been supported by National Key R&D Program of China (2024YFB4205000 and 2024YFB4205004) and National Natural Science Foundation of China (52222212, 52227803, and 52172261). J.S. also gratefully acknowledges support from the Youth Innovation Promotion Association of the Chinese Academy of Sciences (2022006). J.W. acknowledges support from China National Postdoctoral Program for Innovative Talents (BX20250177).

### AUTHOR CONTRIBUTIONS

L.L., J.S., and Q.M. conceived the idea and designed the experiments. L.L. and J.W. performed the experiments and data analysis. Yuan Li participated in experimental optimizations. K.Y., X.X., B.Z., M.J., S.C., T.G., and J.W. participated in material and device characterization. Yiming Li, H.W., H.X., Y. Luo, and D.L. supported the discussion. R.X. supported the DFT calculations. L.L., J.S., and Q.M. participated in writing the manuscript.

### DECLARATION OF INTERESTS

The authors declare no competing interests.

### SUPPLEMENTAL INFORMATION

Supplemental information can be found online at <https://doi.org/10.1016/j.joule.2025.102091>.

Received: April 2, 2025

Revised: June 18, 2025

Accepted: July 21, 2025

## REFERENCES

- Wang, A., Chang, N.L., Sun, K., Xue, C., Egan, R.J., Li, J., Yan, C., Huang, J., Rong, H., Ramsden, C., et al. (2021). Analysis of manufacturing cost and market niches for Cu<sub>2</sub>ZnSnS<sub>4</sub> (CZTS) solar cells. *Sustain. Energy Fuels* 5, 1044–1058. <https://doi.org/10.1039/D0SE01734E>.
- NREL. (2025). Best Research-Cell Efficiency Chart. <https://www.nrel.gov/pv/cell-efficiency.html>.
- Wang, J., Shi, J., Yin, K., Meng, F., Wang, S., Lou, L., Zhou, J., Xu, X., Wu, H., Luo, Y., et al. (2024). Pd(II)/Pd(IV) redox shuttle to suppress vacancy defects at grain boundaries for efficient kesterite solar cells. *Nat. Commun.* 15, 4344. <https://doi.org/10.1038/s41467-024-48850-9>.
- Shi, J., Wang, J., Meng, F., Zhou, J., Xu, X., Yin, K., Lou, L., Jiao, M., Zhang, B., Wu, H., et al. (2024). Multinary alloying for facilitated cation exchange and suppressed defect formation in kesterite solar cells with above 14% certified efficiency. *Nat. Energy* 9, 1095–1104. <https://doi.org/10.1038/s41560-024-01551-5>.
- Huang, J., Lu, Z., He, J., Hu, H., Liang, Q., Liu, K., Ren, Z., Zhang, Y., Yu, H., Zheng, Z., et al. (2023). Intrinsically stretchable, semi-transparent organic photovoltaics with high efficiency and mechanical robustness via a full-solution process. *Energy Environ. Sci.* 16, 1251–1263. <https://doi.org/10.1039/D2EE03096A>.
- Chen, Z., Wang, J., Wu, H., Yang, J., Wang, Y., Zhang, J., Bao, Q., Wang, M., Ma, Z., Tress, W., et al. (2022). A Transparent Electrode Based on Solution-Processed ZnO for Organic Optoelectronic Devices. *Nat. Commun.* 13, 4387. <https://doi.org/10.1038/s41467-022-32010-y>.
- Aydin, E., Ugur, E., Yildirim, B.K., Allen, T.G., Dally, P., Razzaq, A., Cao, F., Xu, L., Vishal, B., Yazmaciyan, A., et al. (2023). Enhanced optoelectronic coupling for perovskite/silicon tandem solar cells. *Nature* 623, 732–738. <https://doi.org/10.1038/s41586-023-06667-4>.
- Yang, Q., Duan, W., Eberst, A., Klingebiel, B., Wang, Y., Kulkarni, A., Lambert, A., Bittkau, K., Zhang, Y., Vitusevich, S., et al. (2024). Origin of sputter damage during transparent conductive oxide deposition for semi-transparent perovskite solar cells. *J. Mater. Chem. A* 12, 14816–14827. <https://doi.org/10.1039/D3TA06654A>.
- Zheng, M., Horowitz, K., Woodhouse, M., Battaglia, C., Kapadia, R., and Javey, A. (2016). III-Vs at scale: a PV manufacturing cost analysis of the thin film vapor-liquid-solid growth mode. *Progress in Photovoltaics* 24, 871–878. <https://doi.org/10.1002/pip.2740>.
- Zhang, Y., Ng, S.W., Lu, X., and Zheng, Z. (2020). Solution-Processed Transparent Electrodes for Emerging Thin-Film Solar Cells. *Chem. Rev.* 120, 2049–2122. <https://doi.org/10.1021/acs.chemrev.9b00483>.
- Kim, A., Won, Y., Woo, K., Jeong, S., and Moon, J. (2014). All-Solution-Processed Indium-Free Transparent Composite Electrodes based on Ag Nanowire and Metal Oxide for Thin-Film Solar Cells. *Adv. Funct. Materials* 24, 2462–2471. <https://doi.org/10.1002/adfm.201303518>.
- Kim, A., Lee, H., Kwon, H.-C., Jung, H.S., Park, N.-G., Jeong, S., and Moon, J. (2016). Fully solution-processed transparent electrodes based on silver nanowire composites for perovskite solar cells. *Nanoscale* 8, 6308–6316. <https://doi.org/10.1039/c5nr04585a>.
- Gahlmann, T., Brinkmann, K.O., Becker, T., Tüchtmann, C., Kreusel, C., van gen Hassend, F., Weber, S., and Riedl, T. (2020). Impermeable Charge Transport Layers Enable Aqueous Processing on Top of Perovskite Solar Cells. *Adv. Energy Mater.* 10, 1903897. <https://doi.org/10.1002/aenm.201903897>.
- Gu, Y., Yin, X., Han, J., Zhou, Y., Tai, M., Zhang, Q., Zhou, Y., Li, J., and Lin, H. (2019). All-Layer Sputtering-Free Cu<sub>2</sub>Zn<sub>1-x</sub>Cd<sub>x</sub>SnS<sub>4</sub> Solar Cell with Efficiency Exceeding 7.5%. *ChemistrySelect* 4, 5979–5983. <https://doi.org/10.1002/slct.201900520>.
- Liu, R., Tan, M., Zhang, X., Xu, L., Chen, J., Chen, Y., Tang, X., and Wan, L. (2018). Solution-processed composite electrodes composed of silver nanowires and aluminum-doped zinc oxide nanoparticles for thin-film solar cells applications. *Sol. Energy Mater. Sol. Cells* 174, 584–592. <https://doi.org/10.1016/j.solmat.2017.09.042>.
- Gu, Y., Yin, X., Han, J., Zhou, Y., Tai, M., Zhang, Q., Li, J., Hao, X., and Lin, H. (2019). All Solution-Processed Cu<sub>2</sub>ZnSnS<sub>4</sub> Solar Cell by Using High-Boiling-Point Solvent Treated Ball-Milling Process with Efficiency Exceeding 6%. *ChemistrySelect* 4, 982–989. <https://doi.org/10.1002/slct.201804028>.
- Edinger, S., Bansal, N., Wibowo, A.R., Winkler, N., Illich, P., Zechmeister, A., Plessing, L., Meissner, D., and Dimopoulos, T. (2019). All-solution-processed transparent front contact for monograin layer kesterite solar cells. *Progress in Photovoltaics* 27, 547–555. <https://doi.org/10.1002/pip.3122>.
- Jiang, Y., Dong, X., Sun, L., Liu, T., Qin, F., Xie, C., Jiang, P., Hu, L., Lu, X., Zhou, X., et al. (2022). An alcohol-dispersed conducting polymer complex for fully printable organic solar cells with improved stability. *Nat. Energy* 7, 352–359. <https://doi.org/10.1038/s41560-022-00997-9>.
- Jiang, X., Song, Z., Liu, G., Ma, Y., Wang, A., Guo, Y.-W., and Du, Z. (2020). AgNWs/AZO composite electrode for transparent inverted ZnCdSeS/ZnS quantum dot light-emitting diodes. *Nanotechnology* 31, 055201. <https://doi.org/10.1088/1361-6528/ab4dcd>.
- Han, Y., Guo, J., Luo, Q., and Ma, C.-Q. (2023). Solution-Processable Zinc Oxide for Printed Photovoltaics: Progress, Challenges, and Prospect. *Adv. Energy Sustainability Res* 4, 2200179. <https://doi.org/10.1002/aesr.202200179>.
- Cai, F., Tu, Y., Tian, D., Fang, Y., Hou, B., Ishaq, M., Jiang, X., Li, M., Wang, S., and Du, Z. (2023). Defect passivation and electron band energy regulation of a ZnO electron transport layer through synergetic bifunctional surface engineering for efficient quantum dot light-emitting diodes. *Nano-scale* 15, 10677–10684. <https://doi.org/10.1039/d3nr01194a>.
- Allen, M.W., and Durbin, S.M. (2008). Influence of oxygen vacancies on Schottky contacts to ZnO. *Appl. Phys. Lett.* 92, 122110. <https://doi.org/10.1063/1.2894568>.
- Kim, J.J., Shuji, K., Zheng, J., He, X., Sajjad, A., Zhang, H., Su, H., and Choy, W.C.H. (2024). Tri-system integration in metal-oxide nanocomposites via in-situ solution-processed method for ultrathin flexible transparent electrodes. *Nat. Commun.* 15, 2070. <https://doi.org/10.1038/s41467-024-46243-6>.
- Kim, M., Jeong, J., Lu, H., Lee, T.K., Eickemeyer, F.T., Liu, Y., Choi, I.W., Choi, S.J., Jo, Y., Kim, H.-B., et al. (2022). Conformal quantum dot-SnO<sub>2</sub> layers as electron transporters for efficient perovskite solar cells. *Science* 375, 302–306. <https://doi.org/10.1126/science.abh1885>.
- Rühle, S. (2016). Tabulated values of the Shockley–Queisser limit for single junction solar cells. *Sol. Energy* 130, 139–147. <https://doi.org/10.1016/j.solener.2016.02.015>.
- Shi, J., Dong, J., Lv, S., Xu, Y., Zhu, L., Xiao, J., Xu, X., Wu, H., Li, D., Luo, Y., and Meng, Q. (2014). Hole-conductor-free perovskite organic lead iodide heterojunction thin-film solar cells: High efficiency and junction property. *Appl. Phys. Lett.* 104, 063901. <https://doi.org/10.1063/1.4864638>.
- Madeira, P.P., Ferreira, L.A., Uversky, V.N., and Zaslavsky, B.Y. (2024). Polarity of Aqueous Solutions. *Liquids* 4, 107–116. <https://doi.org/10.3390/liquids4010005>.
- Azani, M.R., Hassanpour, A., and Torres, T. (2020). Benefits, Problems, and Solutions of Silver Nanowire Transparent Conductive Electrodes in Indium Tin Oxide (ITO)-Free Flexible Solar Cells. *Adv. Energy Mater.* 10, 2002536. <https://doi.org/10.1002/aenm.202002536>.
- Arulraj, A., Ilayaraja, N., Rajeshkumar, V., and Ramesh, M. (2019). Direct Synthesis of cubic shaped Ag<sub>2</sub>S on Ni mesh as Binder-free Electrodes for Energy Storage Applications. *Sci. Rep.* 9, 10108. <https://doi.org/10.1038/s41598-019-46583-0>.
- Jiang, D., Chen, L., Xie, J., and Chen, M. (2014). Ag<sub>2</sub>S/g-C<sub>3</sub>N<sub>4</sub> composite photocatalysts for efficient Pt-free hydrogen production. The co-catalyst function of Ag/Ag<sub>2</sub>S formed by simultaneous photodeposition. *Dalton Trans.* 43, 4878–4885. <https://doi.org/10.1039/c3dt53526f>.
- Pang, M., Hu, J., and Zeng, H.C. (2010). Synthesis, Morphological Control, and Antibacterial Properties of Hollow/Solid Ag<sub>2</sub>S/Ag Heterodimers.

- J. Am. Chem. Soc. 132, 10771–10785. <https://doi.org/10.1021/ja102105q>.
32. Zhao, Y., Gao, L., Wang, Q., Zhang, Q., Yang, X., Zhu, J., Huang, H., Duan, J., and Tang, Q. (2024). Reinforced SnO<sub>2</sub> tensile-strength and “buffer-spring” interfaces for efficient inorganic perovskite solar cells. *Carbon Energy* 6, e468. <https://doi.org/10.1002/cey2.468>.
33. Zhumekenov, A.A., Burlakov, V.M., Saidaminov, M.I., Alofi, A., Haque, M. A., Turedi, B., Davaasuren, B., Dursun, I., Cho, N., El-Zohry, A.M., et al. (2017). The Role of Surface Tension in the Crystallization of Metal Halide Perovskites. *ACS Energy Lett.* 2, 1782–1788. <https://doi.org/10.1021/acsenenergylett.7b00468>.
34. Shi, J., Li, D., Luo, Y., Wu, H., and Meng, Q. (2016). Opto-electro-modulated transient photovoltage and photocurrent system for investigation of charge transport and recombination in solar cells. *Rev. Sci. Instrum.* 87, 123107. <https://doi.org/10.1063/1.4972104>.
35. Cao, L., Wang, L., Zhou, Z., Zhou, T., Li, R., Zhang, H., Wang, Z., Wu, S., Najjar, A., Tian, Q., et al. (2024). Modifying Surface Termination by Bidentate Chelating Strategy Enables 13.77% Efficient Kesterite Solar Cells. *Adv. Mater.* 36, e2311918. <https://doi.org/10.1002/adma.202311918>.
36. Vigil-Galán, O., Andrade-Arzu, J.A., Courel-Piedrahita, M., Mejía-García, C., Valencia-Resendiz, E., Sánchez-González, Y., Espíndola-Rodríguez, M., Saucedo-Silva, E., González-Castillo, R., Rodríguez-González, E., et al. (2017). Study of CBD-CdS/CZTGe solar cells using different Cd sources: behavior of devices as a MIS structure. *J. Mater. Sci. Mater. Electron.* 28, 18706–18714. <https://doi.org/10.1007/s10854-017-7820-7>.
37. Yang, S., and Yu, H. (2023). The modification of ZnO surface with natural antioxidants to fabricate highly efficient and stable inverted organic solar cells. *Chem. Eng. J.* 452, 139658. <https://doi.org/10.1016/j.cej.2022.139658>.
38. Quiñones, R., Shoup, D., Behnke, G., Peck, C., Agarwal, S., Gupta, R.K., Fagan, J.W., Mueller, K.T., Iulucci, R.J., and Wang, Q. (2017). Study of Perfluorophosphonic Acid Surface Modifications on Zinc Oxide Nanoparticles. *Materials (Basel)* 10, 1363. <https://doi.org/10.3390/ma10121363>.
39. Brow, R.K. (1996). An XPS study of oxygen bonding in zinc phosphate and zinc borophosphate glasses. *J. Non-Cryst. Solids* 194, 267–273. [https://doi.org/10.1016/0022-3093\(95\)00500-5](https://doi.org/10.1016/0022-3093(95)00500-5).
40. Chen, Q., Wang, C., Li, Y., and Chen, L. (2020). Interfacial Dipole in Organic and Perovskite Solar Cells. *J. Am. Chem. Soc.* 142, 18281–18292. <https://doi.org/10.1021/jacs.0c07439>.
41. Liu, C., Yang, Y., Chen, H., Xu, J., Liu, A., Bati, A.S.R., Zhu, H., Grater, L., Hadke, S.S., Huang, C., et al. (2023). Bimolecularly passivated interface enables efficient and stable inverted perovskite solar cells. *Science* 382, 810–815. <https://doi.org/10.1126/science.adk1633>.
42. Lou, L., Wang, J., Yin, K., Meng, F., Xu, X., Zhou, J., Wu, H., Shi, J., Luo, Y., Li, D., and Meng, Q. (2023). Crown Ether-Assisted Colloidal ZnO Window Layer Engineering for Efficient Kesterite (Ag,Cu)<sub>2</sub>ZnSn(S,Se)<sub>4</sub> Solar Cells. *ACS Energy Lett.* 8, 3775–3783. <https://doi.org/10.1021/acsenenergylett.3c01329>.
43. Chang, F.M., Brahma, S., Huang, J.H., Wu, Z.Z., and Lo, K.Y. (2019). Strong correlation between optical properties and mechanism in deficiency of normalized self-assembly ZnO nanorods. *Sci. Rep.* 9, 905.
44. Gunawan, O., Todorov, T.K., and Mitzi, D.B. (2010). Loss mechanisms in hydrazine-processed Cu<sub>2</sub>ZnSn(Se, S)<sub>4</sub> solar cells. *Appl. Phys. Lett.* 97, 233506. <https://doi.org/10.1063/1.3522884>.
45. Li, Y., Shi, J., Yu, B., Duan, B., Wu, J., Li, H., Li, D., Luo, Y., Wu, H., and Meng, Q. (2020). Exploiting Electrical Transients to Quantify Charge Loss in Solar Cells. *Joule* 4, 472–489. <https://doi.org/10.1016/j.joule.2019.12.016>.
46. Aydin, E., Altinkaya, C., Smirnov, Y., Yaqin, M.A., Zanon, K.P.S., Paliwal, A., Firdaus, Y., Allen, T.G., Anthopoulos, T.D., Bolink, H.J., et al. (2021). Sputtered transparent electrodes for optoelectronic devices: Induced damage and mitigation strategies. *Matter* 4, 3549–3584. <https://doi.org/10.1016/j.matt.2021.09.021>.
47. Xu, X., Zhou, J., Yin, K., Wang, J., Lou, L., Li, D., Shi, J., Wu, H., Luo, Y., and Meng, Q. (2023). 12.84% Efficiency Flexible Kesterite Solar Cells by Heterojunction Interface Regulation. *Adv. Energy Mater.* 13, 2301701. <https://doi.org/10.1002/aenm.202301701>.
48. Yang, K.-J., Kim, S., Kim, S.-Y., Son, D.-H., Lee, J., Kim, Y.-I., Sung, S.-J., Kim, D.-H., Enkhbat, T., Kim, J., et al. (2021). Sodium Effects on the Diffusion, Phase, and Defect Characteristics of Kesterite Solar Cells and Flexible Cu<sub>2</sub>ZnSn(S,Se)<sub>4</sub> with Greater than 11% Efficiency. *Adv. Funct. Materials* 31, 2102238. <https://doi.org/10.1002/adfm.202102238>.
49. Ahmad, N., Zhao, Y., Ye, F., Zhao, J., Chen, S., Zheng, Z., Fan, P., Yan, C., Li, Y., Su, Z., et al. (2023). Cadmium-Free Kesterite Thin-Film Solar Cells with High Efficiency Approaching 12%. *Adv. Sci. (Weinh)* 10, e2302869. <https://doi.org/10.1002/advs.202302869>.
50. Mao, Y., Wang, T., Jian, Y., Huang, Y., Deng, Y., Gu, E., Lin, X., and Yang, G. (2025). 12.86% Efficient Cu<sub>2</sub>ZnSn(S,Se)<sub>4</sub> Thin Film Solar Cells via Ink-jet Printing with 2-Methoxyethanol-Based Air-Stable Precursor Ink. *Adv. Funct. Mater.* 35, 2416689. <https://doi.org/10.1002/adfm.202416689>.
51. Xu, H., Ge, S., Wang, T., Gu, E., and Lin, X. (2024). Flexible Cu<sub>2</sub>ZnSn(S, Se)<sub>4</sub> thin film solar cells with lithium doping via doctor blading. *Sci. China Mater.* 67, 67–75. <https://doi.org/10.1007/s40843-023-2670-6>.
52. Xu, X., Zhou, J., Yin, K., Wang, J., Lou, L., Jiao, M., Zhang, B., Li, D., Shi, J., Wu, H., et al. (2023). Controlling Selenization Equilibrium Enables High-Quality Kesterite Absorbers for Efficient Solar Cells. *Nat. Commun.* 14, 6650. <https://doi.org/10.1038/s41467-023-42460-7>.
53. Zhou, J., Xu, X., Wu, H., Wang, J., Lou, L., Yin, K., Gong, Y., Shi, J., Luo, Y., Li, D., et al. (2023). Control of the phase evolution of kesterite by tuning of the selenium partial pressure for solar cells with 13.8% certified efficiency. *Nat. Energy* 8, 526–535. <https://doi.org/10.1038/s41560-023-01251-6>.
54. Platzer-Björkman, C., Barreau, N., Bär, M., Choubrac, L., Grenet, L., Heo, J., Kubart, T., Mittiga, A., Sanchez, Y., Scragg, J., et al. (2019). Back and front contacts in kesterite solar cells: state-of-the-art and open questions. *J. Phys. Energy* 1, 044005. <https://doi.org/10.1088/2515-7655/ab3708>.
55. Yin, K., Wang, J., Lou, L., Meng, F., Xu, X., Zhang, B., Jiao, M., Shi, J., Li, D., Wu, H., et al. (2025). Gradient bandgaps in sulfide kesterite solar cells enable over 13% certified efficiency. *Nat. Energy* 10, 205–214. <https://doi.org/10.1038/s41560-024-01681-w>.
56. Tseberlidis, G., Gobbo, C., Trifiletti, V., Di Palma, V., and Binetti, S. (2024). Cd-free kesterite solar cells: State-of-the-art and perspectives. *Sustain. Mater. Technol.* 41, e01003. <https://doi.org/10.1016/j.susmat.2024.e01003>.